Large-scale density functional calculations of the surface properties of the Wigner crystal

R. Cortes-Huerto and P. Ballone

Atomistic Simulation Centre, Queen's University Belfast, Belfast BT7 1NN, United Kingdom

The surface properties of the jellium model have been investigated by large supercell computations in the density functional theory-local spin-density (DFT-LSD) approach for planar slabs with up to 1000 electrons. A wide interval of densities has been explored, extending into the stability range of the Wigner crystal. Most computations have been carried out on nominally paramagnetic samples with an equal number of spin-up and spin-down electrons. The results show that within DFT-LSD spontaneous spin polarization and charge localization start nearly simultaneously at the surface for $r_s \sim 20$, then, with decreasing density, they progress toward the center of the slab. Electrons are fully localized and spin polarized at $r_s = 30$. At this density the charge distribution is the superposition of disjoint charge blobs, each corresponding to one electron. The distribution of blobs displays both regularities and disorder, the first being represented by well-defined planes and simple in-plane geometries, and the latter by a variety of surface defects. The surface energy, surface dipole, electric polarisability, and magnetization pattern have been determined as a function of density. All these quantities display characteristic anomalies at the density of the localization transition. The analysis of the low-frequency electric conductivity shows that in the fluid paramagnetic regime the in-plane current preferentially flows in the central region of the slab and the two spin channels are equally conducting. In the charge localized, spin-polarized regime, conductivity is primarily a surface effect, and an apparent asymmetry is observed in the two spin currents.

The one-component plasma (OCP) consisting of quantum electrons in a fixed external potential is arguably one of the most fundamental many-body models,[1,2] whose detailed understanding is a prerequisite for a broad spectrum of theoretical and computational developments, ranging from density functional theory[3] to electron dynamics and spectroscopy.[4] The overall picture of the OCP phase diagrams includes a paramagnetic fluid phase at high density, and a crystal phase (Wigner crystal[5]) at low density, separated by a spin-polarized fluid phase.[6–8] The density at which the phase transitions among these phases take place, however, are much lower than those of valence electrons in simple metals, and until recently the stability and properties of the Wigner crystal have been considered primarily as a conceptual curiosity.

New experimental developments have made it possible to approach the low densities at which the Wigner crystal is expected to arise, providing tantalizing evidence of its existence,[9] especially for systems made of electrons or holes confined in two-dimensional (2D) layers[10] and in nanowires.[11,12] These results, in turn, provide motivations for investigating Wigner crystal properties and to extend the scope of research to all features that might affect experimental results. Surfaces, in particular, are a necessary component of every real system and therefore understanding how a Wigner crystal of finite dimension is terminated is now a relevant issue.

The simplest and most popular version of OCP is represented by the so-called jellium model, in which the external potential confining the electrons is due to the Coulomb interaction of the electrons with a rigid background of positive charge, whose density is constant (ρ_b) within a predefined volume, and zero outside. The background density ρ_b is often expressed in terms of the so-called Wigner-Seitz radius r_s, which measures (in atomic units) the radius of the sphere containing, on average, one electron, giving $1/\rho_b = 4\pi r_s^3/3$.

The surface properties of such a model have been extensively investigated since the early days of the quantum-mechanical theory of solids.[13] More recent studies relied on density functional theory (DFT),[14–16] on quantum Monte Carlo,[17,18] and on a variety of other many-body techniques (see, for instance, the Fermi hypernetted chain computations of Ref. [19]). To the best of our knowledge, however, surface computations have been limited to fairly high densities, corresponding to the simple (alkali) metal range, i.e., $2 < r_s < 6$.

The surface properties of low-density jellium in the stability range of the Wigner crystal are virtually unexplored but they might be expected to reflect the structure of the underlying crystal phase. Even though the quantitative details of the low-density portion of the [extended three-dimensional (3D)] OCP phase diagram are still (at least partly) the subject of debate,[20] the most recent quantum Monte Carlo studies[21] find the body-centered cubic (bcc) lattice to be the ground-state structure over the entire density range for which the Wigner crystal is stable. However, the fcc lattice is very close in energy[8] and different spin configurations are impossible to resolve in the crystal phase[22] to within the error bar of practical quantum Monte Carlo (QMC) computations.[23] Therefore, one might expect the (100) surface of bcc to dominate the picture,[24] with perhaps a subsidiary role for the fcc(111) surface, appearing either as a metastable feature, or being stabilized by the anisotropy at the background edge. Other structures, however, might also appear as a consequence of finite size and of other geometric factors such as the aspect ratio of the slab. For completeness, and considering that our systems are somewhat in between 2D and 3D, we mention that several QMC computations of the 2D electron gas ground-state properties have been carried out in recent years.[25] The results point to a transition from the paramagnetic to the ferromagnetic fluid at $r_s = 20$ while

Wigner crystallization takes place at $r_s=34$ (see also Ref. 1, page 53).

Recently, Teraoka and co-workers[26] carried out a series of computations for quasi-2D jellium films, exposing two planar surfaces. All these studies were based on density functional theory, in most cases relying on the local density approximation [density functional theory-local spin density (DFT-LSD)].[3] Solutions have been obtained under simplifying conditions, constraining the Kohn-Sham (KS) orbitals to be plane waves in the directions (x,y) parallel to the surface. These computations predict a broad and unexpected variety of ground-state geometries and especially of spin configurations for jellium slabs, suggesting a much richer picture than considered until now. Computations by the same group[27] (see also Ref. 28) for the *extended* 3D jellium model using a similar approach have also predicted a variety of unexpected phases, including sequences of alternating high-density and low-density planes, rods, and finally, localized electron dots arranged on the bcc lattice. We emphasize again that, both for the quasi-2D and for the 3D cases, solutions have been obtained under constraints imposed only for computational convenience, and the proposed ground-state configurations were identified by comparing a predefined and limited set of different possibilities.

We present in this paper the results of an extensive set of DFT-LSD computations for the same planar slab geometry, using large supercells with up to 1000 electrons, expressing Kohn-Sham orbitals on a large basis of plane waves and minimizing the DFT-LSD functional without constraints. Our objective is to characterize surface properties of the Wigner crystal. To this aim, we explore a wide interval of densities from $r_s=10$ to $r_s=40$, covering the range at which spin polarization and charge localization take place within DFT-LSD. We investigate, in particular, the spin- and electron-density distributions, we identify and characterize the charge localization transition, and we compute properties such as the surface energy, electron conductivity parallel to the surface, and density of states for the Kohn-Sham eigenvalues. Our results do not reflect the same sequence of successive phase transitions and exotic structures suggested in Refs. 26 and 27, but confirm that, at least according to the DFT-LSD approximation, the transformation from the liquid to the crystal phase is a complex process taking place in stages. According to our computations, spin polarization and localization start virtually simultaneously at the surface, and then, with decreasing density, they propagate inwards. Moreover, and perhaps more interestingly, the ground-state structures found by our simulations display a number of apparent defects. In part, these might arise from the finite effort applied to optimize the ground-state electron density. However, they mainly reflect the near degeneracy of many different structures, a feature that is likely to be important also in real systems.

In discussing these DFT-LSD results it is important to bear in mind that the picture provided by this approach might differ even qualitatively from the one (not available yet) that would be provided by QMC, arguably representing the natural benchmark for this kind of systems. Quantum MC and DFT-LSD already disagree on the phase diagram of the extended 3D jellium model. All transition densities predicted by DFT-LSD, for instance, are much higher (lower r_s) than those given by QMC computations.[29] Even more importantly, the transitions described by DFT-LSD differ qualitatively from those predicted by QMC. For instance, while QMC predicts two distinct transitions from the paramagnetic to (partially spin polarized) ferromagnetic fluid, and then from this last to the Wigner crystal, DFT-LSD predicts spin polarization and charge localization to arise simultaneously, and to proceed fairly gradually. A simultaneous charge localization and (antiferromagnetic) spin-polarization transition is predicted also by Hartree-Fock, which, however, locates this combined phase change at $r_s=4.4$ in 3D, and at $r_s=1.44$ in 2D.[30]

These observations might suggest again that the DFT-LSD results are simply a theoretical curiosity, without a close relation with the exact result for the underlying model, not to mention real systems. However, this conclusion is premature since no QMC data for the 3D OCP is the result of an unconstrained relaxation of the system toward its ground state. Transition densities, in particular, have been determined by comparing the energy of a small set of different solutions that might not include the most relevant ones. In particular, the types of partially spin-polarized and weakly localized ground-state orbitals predicted by DFT-LSD have never been considered in QMC computations. Moreover, it might be interesting to note that going from LSD to gradient corrections, supposedly a more refined exchange-correlation approximation, gives results even farther from the QMC ones.[31]

For all the reasons listed in the last paragraph, we present here the DFT-LSD results for the surface of the Wigner crystal, aiming at stimulating computations by other methods, and especially by QMC. Understanding Wigner crystal properties, and its surface properties, in particular, could provide a stringent test of any DFT approximation meant to describe electron systems at high correlation. Already at this stage, however, we think that DFT-LSD data will contain at least part of the truth since the scheme accounts for all the important energy contributions even though some quantitative details might still be inaccurate.

I. MODEL AND THE COMPUTATIONAL METHOD

The model we use consists of an inhomogeneous version of the well-known jellium model.[2] A system of $N=N_{up}+N_{down}$ electrons is contained in a cubic simulation box of side L, and confined by the electrostatic potential $V_b(\mathbf{r})$ of an orthorhombic positive charge distribution of sides $L_x=L_y=L$, and $L_z=\alpha L < L$. The system is periodically replicated in 3D, giving rise to a planar slab of thickness αL extended along xy, separated from its nearest periodic replicas in the z direction by an empty region of space whose width is $(1-\alpha)L$. In the computations reported below, α is either 0.5 or 0.7. In what follows, the background density ρ_b is expressed in terms of the Wigner-Seitz radius r_s. The system is globally neutral, having: $\alpha \rho_b L^3 = N$.

The system periodicity defines a cubic first Brillouin zone in reciprocal space, whose sides are inversely proportional to L. We use large simulation cells with up to 1000 electrons, resulting into a tiny first Brillouin zone that we sample at a single ($\mathbf{k}=0$) point.

According to density functional theory in the KS formulation, the ground-state energy and electron density $\rho(\mathbf{r})$ are determined by minimizing the functional

$$E[\rho] = -\frac{1}{2}\sum_{i=1}^{N}\langle\psi_i|\nabla^2|\psi_i\rangle + \int V_b(z)\rho(\mathbf{r})d\mathbf{r}$$
$$+ \frac{1}{2}\int\frac{\rho(\mathbf{r})\rho(\mathbf{r}')}{|\mathbf{r}-r'|}d\mathbf{r}d\mathbf{r}' + U_{XC}[\rho] \qquad (1)$$

with respect to the occupied single-electron KS orbitals $\{\psi_i, i=1,N\}$. The electron density is expressed as

$$\rho(\mathbf{r}) = \rho_{up}(\mathbf{r}) + \rho_{down}(\mathbf{r}) = \sum_{i=1}^{N_{up}}|\psi_i(\mathbf{r})|^2 + \sum_{i=N_{up}+1}^{N_{up}+N_{down}}|\psi_i(\mathbf{r})|^2. \qquad (2)$$

In what follows, the exchange-correlation energy $U_{XC}[\rho]$ is given by the local spin-density approximation

$$U_{XC}[\rho] = \int\rho(\mathbf{r})\epsilon_{XC}[\rho(\mathbf{r}),\zeta(\mathbf{r})]d\mathbf{r}, \qquad (3)$$

where

$$\zeta(\mathbf{r}) = \frac{\rho_{up}(\mathbf{r}) - \rho_{down}(\mathbf{r})}{\rho_{up}(\mathbf{r}) + \rho_{down}(\mathbf{r})}. \qquad (4)$$

We use for $\epsilon_{XC}[\rho,\zeta]$ the interpolation given in Ref. 32.

In our plane-wave code, the confining electrostatic potential of the background is dealt with in reciprocal space. The Fourier transform of $V_b(\mathbf{r}) \equiv V_b(z)$ is easily obtained from the Fourier transform of the background charge density

$$\widetilde{\rho}(G_z) = \begin{cases} \alpha\rho_b, & \text{if } G_z = 0 \\ 2\dfrac{\rho_b}{L}G_z\sin\left(G_z\dfrac{\alpha L}{2}\right) & \text{if } G_z \neq 0. \end{cases} \qquad (5)$$

Previous QMC computations for jellium spheres[33] have shown that for electron densities in the simple metal range $(2 \leq r_s \leq 6)$ LSD provides energies and electron densities in excellent agreement with the QMC data. No comparison has been made for finite jellium systems at significantly lower density, and, as stated in the introduction, the usage of LSD in this regime is meant to provide predictions to be verified by higher accuracy methods.

The minimization of Eq. (1) is carried out by expanding KS orbitals on a plane wave basis

$$\psi_i(\mathbf{r}) = \sum_{\mathbf{G}} c_{\mathbf{G}} e^{i\mathbf{G}\cdot r}, \qquad (6)$$

where the $\mathbf{G}$'s are reciprocal lattice vectors for the lattice defined by the simulation cell periodicity. The sum extends over all $\mathbf{G}$ vectors whose square norm G^2 is less than a cut-off energy E_{cut}. In what follows, we set $G^2 r_s^2 = 28$ Ry, in such a way to obtain at all densities a constant relative resolution within the simulation cell. For systems of 700 electrons this choice corresponds to a basis of ~ 15000 plane waves per KS orbitals while the electron density is expanded on a basis of 120×10^3 plane waves. Tests carried out for smaller systems and higher cutoff have confirmed the convergence of energies and densities at the cut-off of the main computations.

Expansion (6) transforms the functional variation of Eq. (1) into an algebraic minimization problem.[34] This last is solved by a slight adaptation of the well-known steepest descent method.[35] Each minimization step consists of three energy evaluations along a fixed direction in the space of the $\{c_{\mathbf{G}}^{(i)}\}$ coefficients. The fixed direction is given by the gradient $\partial E_{KS}/\partial c_{\mathbf{G}}^{(i)}$ evaluated at the starting point. The sampling of the KS functional along this direction is carried out at fixed intervals of amplitude δt, each time updating the coefficients $\{c_{\mathbf{G}}\}$ according to

$$c_{\mathbf{G}}^{(i)}[\text{new}] = c_{\mathbf{G}}^{(i)}[\text{old}] - \delta t\frac{\partial E_{KS}}{\partial c_{\mathbf{G}}^{(i)}}, \qquad (7)$$

where δt, whose name is meant to evoke an elementary step of time evolution, is chosen *a priori* and given in input. After each displacement, and before computing the energy, the full set of coefficients is orthogonalized by a Gram-Schmidt routine. This step is still relatively inexpensive ($\sim 5\%$ of the total time) for systems of up to 1000 electrons.

The three energies computed along the fixed direction $\partial E_{KS}/\partial c_{\mathbf{G}}^{(i)}$ are interpolated by a parabola, whose minimization (whenever possible) provides an estimate of the minimum location along the gradient direction. At the beginning of the computation, such a minimization might not be possible since far from the target minimum the parabolic interpolation might have a minimum instead of a maximum. In such a case, the search is continued in regular steps of amplitude δt. This problem, however, arises only at the beginning while the interpolation-minimization approach is stable in the lengthy stage of refinement.

As already mentioned, the minimization approach described above is a slight modification of the steepest descent method. Standard computational textbooks[35] state and demonstrate that other approaches such as conjugate gradient are more efficient. While this is certainly the case, in principle, it might not be the case in practice. It is worth mentioning, for instance, that conjugate gradient differs significantly from steepest descent only on sequences of minimization steps whose length (n_{steps}) is comparable to the number of variables to be minimized. In our minimizations, n_{steps} is always much smaller than the (very large) number of variables. Moreover, standard implementations of conjugate gradient and steepest descent require the accurate minimization of the energy along one direction, a task that is often fairly time consuming. Our simple approach based on interpolation and minimization avoids this accurate line minimization step. As a result, when judged on the rate of energy decrease per equal CPU time, our simple approach outperforms current implementations of conjugate gradient in plane wave codes.

For our systems, the minimization of the energy to better than six digits requires a few days on a single Opteron CPU and thus it represents only a modest computational requirement. Needless to say, we find only local minima, while reaching the absolute (ground-state) minimum is not guaranteed. This limitation, however, is shared by all practical computational method. Moreover, its impact on computed prop-

erties is fairly mild, since the competing minima are nearly degenerate, and also their geometric and magnetic structures are similar.

Once the ground-state orbitals, electron density, and KS potentials have been determined, empty states are computed by minimizing the auxiliary functional

$$K_{empty}[\{\psi^{(e)}(\mathbf{r})\}] = \sum_{i=1}^{N'_{up}} \langle \psi_i^{(e)}(\mathbf{r}) | -\frac{1}{2}\nabla^2 + V_{up}(\mathbf{r}) | \psi_i^{(e)}(\mathbf{r}) \rangle$$
$$+ \sum_{i=N'_{up}+1}^{N'_{up}+N'_{dn}} \langle \psi_i^{(e)}(\mathbf{r}) | -\frac{1}{2}\nabla^2 + V_{down}(\mathbf{r}) | \psi_i^{(e)}$$
$$\times (\mathbf{r}) \rangle \qquad (8)$$

with respect to the Fourier coefficients defining the additional $\{\psi_i^{(e)}\}$ orbitals. In Eq. (8), $V_{up}(\mathbf{r})$ and $V_{down}(\mathbf{r})$ are the ground-state Kohn-Sham potentials for spin-up and spin-down electrons, respectively, and N'_{up} and N'_{down} are the number of spin-up and spin-down orbitals to be determined. The two potentials $V_{up}(\mathbf{r})$ and $V_{down}(\mathbf{r})$ depend only on the density and spin polarization of the occupied orbitals, and are kept fixed during this stage of the computation. Empty states of equal spin are orthonormal among themselves and normalized to all occupied states of the same spin.

The dipole polarizability along the direction z perpendicular to the slab surface has been computed by reoptimizing the electron density upon applying a weak, piece-wise linear perturbing potential. The corresponding electric field is constant along the entire width of the background slab, plus a safety margin on each side of width $(1-\alpha)L/4$. The applied field reverses its sign in the remaining slice of (nearly) empty space of width $(1-\alpha)L/2$. The induced dipole per unit area is

$$P_z = -e \int_{-L/2}^{L/2} [\rho(z) - \rho_b(z)] z \, dz, \qquad (9)$$

where the notation $\rho_b(z)$ indicates that the background density only extends over a portion (αL) of the simulation cell. The expression for P_z is evaluated in Fourier space.

The electric conductivity parallel to the slab surface is computed using the Kubo-Greenwood expression[3]

$$\sigma_{\parallel}(\omega) = \frac{2\pi}{L^3} \sum_{i,j} |D_{ij}|^2 \frac{n_0(\epsilon_i) - n_0(\epsilon_j)}{\omega} \delta(\epsilon_i - \epsilon_j - \omega), \quad (10)$$

where n_0 are ground state occupation numbers, and the sum extends over occupied and empty states. The current parallel to the surface induced by an external field E_x, constant in space and oscillating at frequency ω in time, is given by

$$J_x(\omega) = \frac{2\pi E_x}{L^3} \sum_{i,j} |D_{ij}|^2 \frac{n_0(\epsilon_i) - n_0(\epsilon_j)}{\omega} \delta(\epsilon_i - \epsilon_j - \omega). \tag{11}$$

Matrix elements contributing to the current are of the form

$$D_{ij} = \int d\mathbf{r} [\psi_i^{(e)}(\mathbf{r})]^* \nabla_x \psi_j(\mathbf{r}) = \int dz \Delta_{ij}(z), \qquad (12)$$

where

$$\Delta_{ij}(z) = \int dx\,dy [\psi_i^{(e)}(\mathbf{r})]^* \nabla_x \psi_j(\mathbf{r}). \qquad (13)$$

Using this definition we rewrite Eq. (11) as

$$J_x(\omega) = \frac{2\pi E_x}{L^3} \sum_{i,j} \int dz |\Delta_{i,j}(z)|^2 \frac{n_0(\epsilon_i) - n_0(\epsilon_j)}{\omega} \delta(\epsilon_i - \epsilon_j - \omega)$$
$$= \int dz J_z(\omega, z), \qquad (14)$$

where we defined

$$J_x(\omega, z) = \frac{2\pi E_x}{L^3} \sum_{i,j} |\Delta_{i,j}(z)|^2 \frac{n_0(\epsilon_i) - n_0(\epsilon_j)}{\omega} \delta(\epsilon_i - \epsilon_j - \omega).$$
$$(15)$$

The distribution $J(z, \omega)$ can be interpreted as the induced current flowing along the plane of constant z, driven by the field E_x. This interpretation will be used in the following section to characterize the space distribution of conductivity.

II. RESULTS

Computations have been carried out over a wide range of densities from $r_s = 10$ to $r_s = 40$, focusing especially on the low-density cases ($r_s \geq 20$). Most of the results presented below concern systems of $N = 700$ electrons. This number does not correspond to the filling of degenerate shells of plane wave states or to the regular arrangement of particles on a simple lattice. Such a choice is meant to provide results unbiased toward any specific phase that is expected to be relevant for our system. On the other hand, it also implies that our systems are open shells with respect to the orbital quantum numbers, and this feature will be reflected in the precise location of the Fermi energy within (instead of in between) electron bands, and it will also affect the computation of conductivity. The results obtained for $N = 700$ have been verified by computations for systems of $N = 512$ and $N = 1000$ electrons for selected r_s values. The systems we investigate are globally spin compensated, having $N_{up} = N_{down}$. Spin polarization, however, can arise locally as a way to decrease the total energy by enhancing the exchange interactions. The effect of global spin polarization has been assessed by carrying out computations for a fully spin-polarized sample at $r_s = 40$ and $N = 700$. At this density, the slab thickness is ~20 nm.

The dependence of the electron density profile on the slab thickness at constant ρ_b is displayed in Fig. 1 while Fig. 2 shows its dependence on the background density ρ_b at constant size ($N = 700$) of the system. In all cases, the electron-density profile in the direction z perpendicular to the surface displays the characteristic oscillations and the (relatively small) electron spill out made familiar by a large number of studies of planar jellium surfaces available in the literature.[14] The density oscillations extending up to the center of the slab
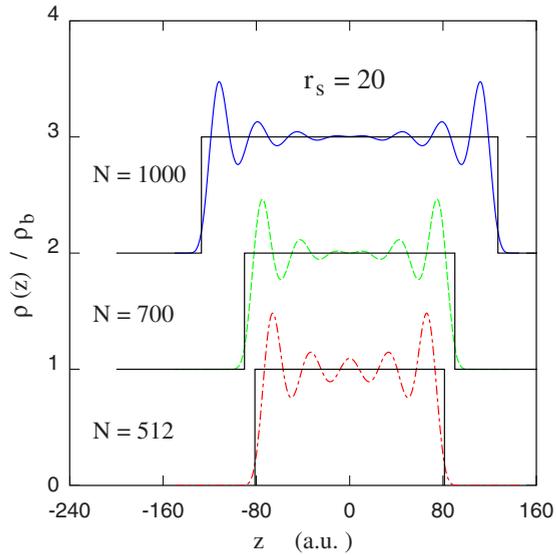
FIG. 1. (Color online) Electron density profile along the direction z perpendicular to the slab surface for $r_s = 20$ and three different system sizes. The curves for $N = 700$ and $N = 1000$ have been shifted along the y direction by one and two units, respectively, for the sake of clarity.

show that, even for $N = 1000$ electrons in the liquid phase, the two planar surfaces are not completely decoupled. However, it is also apparent from Fig. 3 that the density profile in proximity of the edge of the background is fairly well converged already for $N = 700$ electrons. As expected, the amplitude of the density oscillations increases with decreasing density, emphasizing the well-known tendency to localize and order in going toward low-density (high r_s) systems.

Up to $r_s = 20$, no violation of planarity is observed along xy and no spontaneous spin polarization is found in nominally paramagnetic samples ($N_{up} = N_{down}$) apart from low-amplitude wavelike features that arise from filling shells of degenerate of nearly degenerate states.
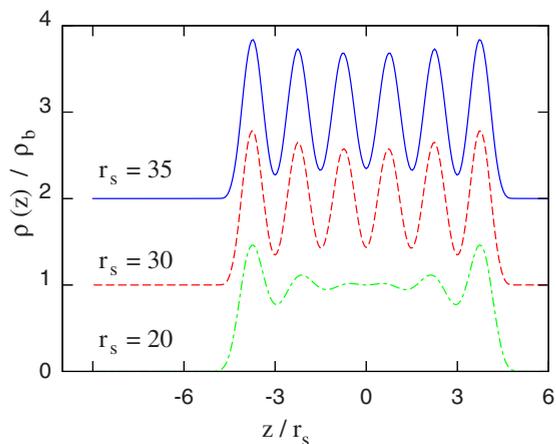
FIG. 2. (Color online) Electron-density profile along the direction z perpendicular to the slab surface for systems of $N = 700$ electrons at three different values of the background density. The curves for $r_s = 30$ and $r_s = 35$ have been shifted along the y direction by one and two units, respectively, for the sake of clarity.
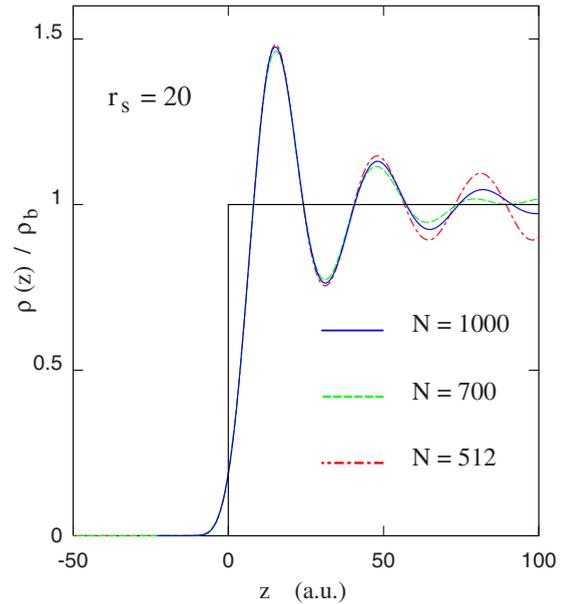
FIG. 3. (Color online) Density profiles of Fig. 1 shifted along the z direction to superimpose the background edge at $z = 0$.

The picture changes gradually but fairly rapidly in the $20 \leq r_s \leq 25$ range, over which charge modulation along xy (see Fig. 4) and spin polarization (see Fig. 5; note in this figure the different value of the isosurfaces for different r_s values) arise simultaneously. Both features at first appear to be localized at the surface and then they progressively propagate toward the inside of the slab, as shown, for instance, by magnetization profiles $[m(\mathbf{r}) = \rho_{up}(\mathbf{r}) - \rho_{down}(\mathbf{r})$, see Fig. 6] and confirmed by density- and spin-polarization isosurfaces.

In the proximity of the transition, the identification of relevant patterns is difficult since charge and spin features change rapidly with decreasing background density, and, moreover, the geometry of charge and spin isosurfaces also depends on the specific value chosen to draw them. None of the patterns seen in our results, however, can be unambiguously identified with the planes and lines discussed in Ref. 26, obtained upon introducing simplifying constraints in the minimization of the KS energy functional. Nevertheless, our computations agree with those of Ref. 26 in highlighting that, at least at the DFT-LSD level of approximation, the change from the paramagnetic fluid to the charge localized, spin-polarized state is a continuous transition, taking place over a density range spanning $20 \leq r_s \leq 25$. Moreover, it is apparent that it represents a complex, multistage transformation, especially as seen at a sharp interface.

The surface energy of the OCP slab has been computed by subtracting the energy of the extended system from the total energy of the slab at equal number of electrons and dividing by twice the area $A = L_x^2$ of each of the two parallel surfaces. For consistency, and to account for the spin-polarization and localization transitions, the total energy of the extended system, having a homogeneous background, has been computed with the method of Sec. I, using the same number of electrons and the same plane-wave cutoff of the slab computations. In the Wigner crystal phase, total energies are dominated by the potential (Madelung) energy. At constant
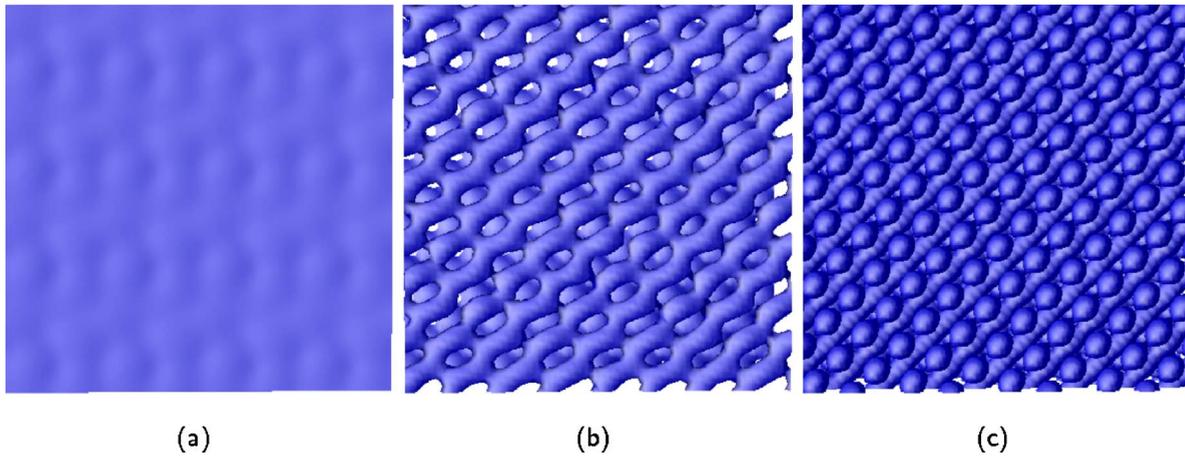
FIG. 4. (Color online) Electron density isosurfaces [at $\rho(\mathbf{r})=\bar{\rho}=1.8\rho_b$] seen from the z direction perpendicular to the slab surface. (a) $r_s=20$; (b) $r_s=25$; and (c) $r_s=30$.

number of electrons N, therefore, the total energy difference ΔE_s between the slab and the system extended in 3D will scale as $1/r_s$. The surface energy u_s, representing the energy difference per unit area, will scale as $1/r_s^3$ (see also Ref. 36). At higher density, in the paramagnetic and spin-polarized phase, potential energy is supplemented by a sizable kinetic-energy contribution, which scales as $1/r_s^2$, giving an $1/r_s^4$ term in the surface energy. A plot of $r_s^3 \times u_s$, therefore, is expected to display a constant plateau at r_s beyond the localization transition while at lower r_s the same function will behave as $r_s^3 \times u_s \sim a + b/r_s$. The plot of $r_s^3 \times u_s$ using the

simulation results for u_s is shown in Fig. 7 and confirms our expectation. Oscillations of the results around the analytical fit for $r_s < 30$ are a manifestation of shell effects and thus arise primarily from kinetic energy.

At all densities such that $r_s \geq 10$, the z dependence of the electrostatic and exchange-correlation potentials display marked oscillations in proximity of the background edge that extend to the entire slab for $r_s > 25$. A suitable averaging procedure (macroscopic averaging[37]) allows us to compute reliable (average) values for the depth $\bar{v}_{XC}$ of the exchange correlation potential well. Together with the corresponding
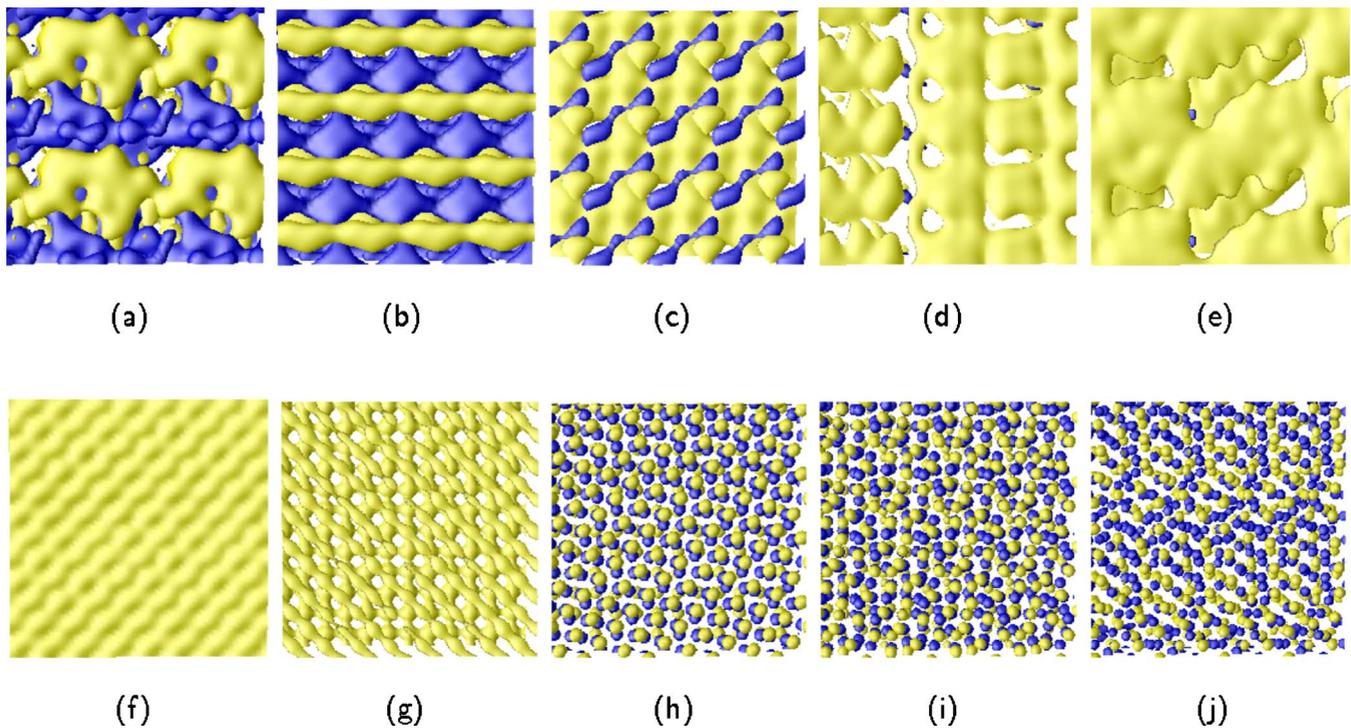
FIG. 5. (Color online) Spin-polarization isosurfaces [at $|m(\mathbf{r})|=\bar{m}$] seen from the z direction perpendicular to the slab surface. (a) $r_s=15$, $\bar{m}=0.02\rho_b$; (b) $r_s=17$, $\bar{m}=0.05\rho_b$; (c) $r_s=20$, $\bar{m}=0.1\rho_b$; (d) $r_s=21$, $\bar{m}=0.1\rho_b$; (e) $r_s=22$, $\bar{m}=0.15\rho_b$; (f) $r_s=25$, $\bar{m}=0.55\rho_b$; (g) $r_s=27$, $\bar{m}=1.3\rho_b$; (h) $r_s=30$, $\bar{m}=2\rho_b$; (i) $r_s=32$, $\bar{m}=2.5\rho_b$; and (j) $r_s=35$, $\bar{m}=3\rho_b$. Dark (blue) surfaces: spin-up and light (yellow) surfaces: spin-down polarization.
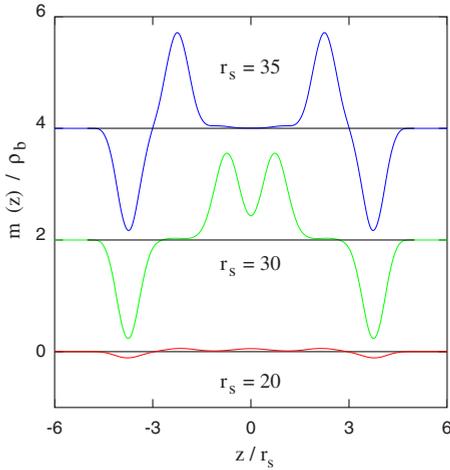
FIG. 6. (Color online) Magnetization profile along the direction z perpendicular to the slab surface for nominally paramagnetic slabs of $N_{up}=N_{dn}=350$ at three different values of the background density.

electrostatic potential drop $\Delta\phi=-e[\phi(\infty)-\phi(0)]$ (where $z=0$ is the center of the slab) this defines the surface work function W_f. Over a wide density range, $r_s\times W_f$ turns out to be nearly constant ($r_s\times W_f\sim20$ eV for $10\leq r_s\leq40$). Nevertheless, a slight anomaly is apparent in the r_s dependence of W_f at $r_s=30$, marking the full crystallization of the entire sample. At variance from what is found at simple metal densities ($2\leq r_s\leq6$), the exchange-correlation and the electrostatic terms entering the definition of W_f are of opposite sign, but the electrostatic term is fairly small, corresponding to $\sim20\%$ (in absolute value) of $\bar{v}_{XC}$.

The number n_{out} of electrons spilling out of the background edge has been computed and the results are shown in the inset of Fig. 7. At all densities n_{out} is small and decreases
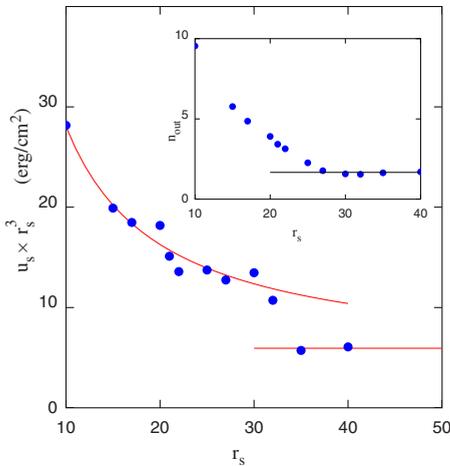
FIG. 7. (Color online) Dependence of the surface energy on r_s. Solid dots: computational results. Full lines: interpolation of $r_s^3\times u_s$ by $a+b/r_s$ at low r_s and by a constant at high r_s. Inset: number n_{out} of electrons spilling out of the background edge as a function of r_s. The data refer to the entire simulated sample and to both sides of the slab. Solid dots: computational results. Full line: fit of the low density (high r_s values) by a constant value.
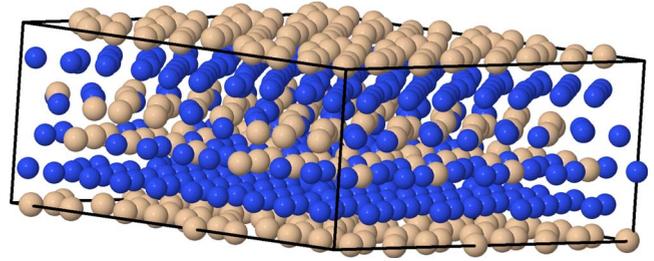
FIG. 8. (Color online) Electron and spin configuration determined by placing spherical particles at local maxima of the spin-up and spin-down densities (see text) for $r_s=30$, $N=1000$. Dark (blue) particles: spin up and light (brown) particles: spin down.

slowly with increasing r_s. Following localization, spill out remains nearly constant thus providing an additional diagnostic sign to monitor localization.

Starting from $r_s=30$, isosurfaces of relatively high electron density ($\rho\sim3\rho_b$) display a distribution of discrete blobs, that can be identified with single electrons, since each of these blobs contains nearly exactly one electron (mean-square deviation of about 2%) and, with an error of a few units at most, we find as many blobs as electrons in the system. Moreover, each blob is spin-polarized, supporting the identification of blobs with single electrons. On the other hand, it is important to remark that individual blobs do not correspond to one single KS eigenstate, but result from the superposition of contributions from at least a few KS orbitals, extending over small clusters consisting of 6–8 blobs. In a few cases, KS orbitals are divided into two or more disconnected regions, participating into non-nearest-neighbor blobs.

To emphasize the close correspondence of blobs and single electrons, we associate a spherical particle to each blob, locating it at the local maximum of the density distribution. As already mentioned, the number of particles distributed in this way over the entire system corresponds very much to N and greatly helps in identifying the charge and spin structures.

The result of this construction for $r_s=30$ is shown in Fig. 8. The distribution of particles turns out to be rather regular, with a sequence of planes parallel to the surface, and a fairly symmetric in-plane structure. A closer inspection, however, reveals a number of defects and anomalies that represent in fact the most interesting result of our structural determination.

First of all, surface vacancies are apparent since the system sizes we use do not necessarily correspond to the filling of an integer number of electron layers. Possibly because of that, at all densities such that charge is localized, the outermost planes tend to be the most disordered of the entire slab since vacancies tend to migrate to the surface. The irregularity in the Kohn-Sham potential due to surface vacancies is likely to be responsible for the splitting of a few blobs into dumbbell distributions, pointing to tunneling centers for the electrons at the surface. In a few extreme cases, the dumbbell geometry is replaced by a spherocylinder charge distribution, whose major axis is on the order of the electron-electron separation, i.e., $\sim2r_s$. An example of this last case is shown
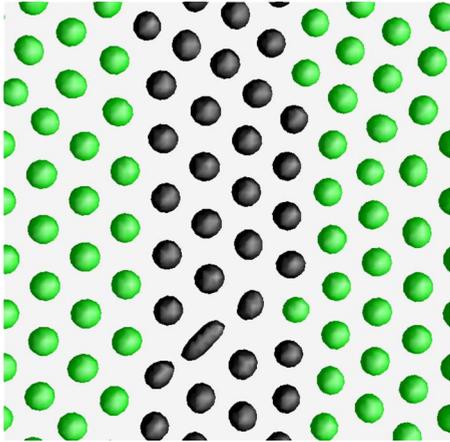
FIG. 9. (Color online) Spherocylindrical charge blob located at a surface vacancy site. Dark (black) blobs: spin-up polarization. Light (green) blobs: spin-down polarization.

in Fig. 9 (which also displays an additional example of surface dislocation).

Intrinsic defects such as vacancies, and low restoring forces at the surface are also responsible for a wide variety of more complex defects, including localized and extended ones. As an example, a closely bound pair made of a positive (A) and a negative (B) disclination, giving rise to a 2D dislocation,[38] is shown in Fig. 10.

At densities close to the localization transition, the Wigner crystal (as given by LSD computations) is supposed to be stable in the bcc structure, whose most stable termination is the (100) surface. A (100) surface geometry is in fact apparent in Fig. 11(a), showing the distribution of particles on the uppermost electron layer for the $r_s = 30$, $N = 700$ sample. The opposite surface, however, displays the characteristic (111) surface structure familiar from face-centered cubic (fcc) or hexagonal close-packing crystals [see Fig. 11(b)]. In the case of the $r_s = 30$, $N = 700$ sample, the matching of the two competing structures takes place in the first layer below the (100) surface (i.e., most of the system is in the fcc structure), that appear to be fairly poorly defined. To emphasize the role of defects in the structure of the simulated slabs, we report that we observed samples displaying the regular alternation of compact fcc(111) planes and of bcc(100) planes throughout the entire slab.

The spin distribution is also fairly defective, different from one sample to the other, and even within each sample it
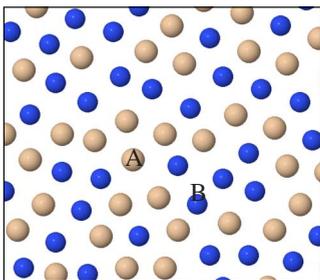
FIG. 10. (Color online) (a) Positive and (b) negative disclination pair, giving rise to a surface (2D) dislocation. Blue (dark) particles: spin-up electron and gray (light) particles: spin-down electrons.

upper surface
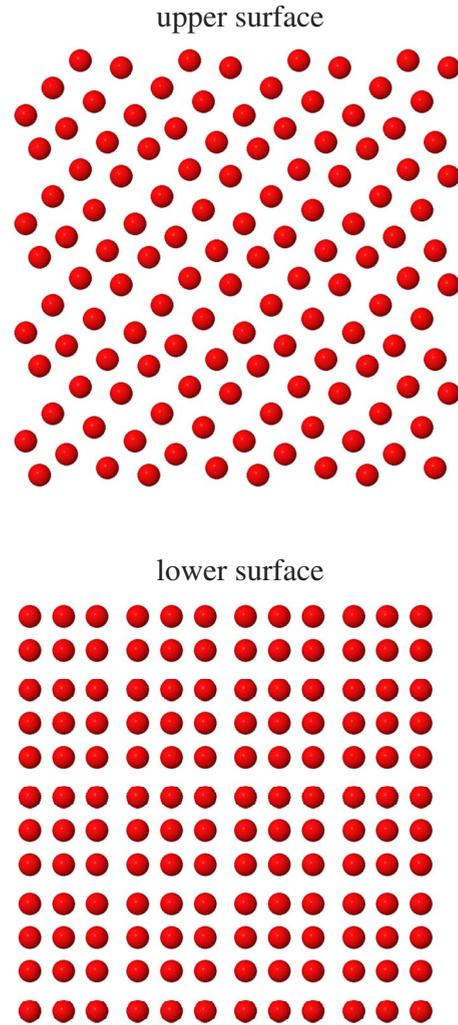
lower surface

FIG. 11. (Color online) Structure of the upper and lower surface of the $r_s = 30$, $N = 700$ sample. Particles represent electron density blobs, distributed according to the procedure described in the text. All surface blobs have the same spin in this sample.

is possible to detect apparent irregularities. The distribution of spin in space tends to be more regular at low r_s than at high r_s, probably because the exchange energy decreased with increasing r_s, and because at low-density systems tend to give rise to glassy configurations already in the space coordinates.

While a few of the localized defects such as surface vacancies might be intrinsic, being due to the incomplete filling of planes, the majority of the defects that we observe might result from a finite effort to locate the absolute minimum of potential energy as a function of the spin and density distributions. A fully exhaustive search, of course practically infeasible, might in fact turn out more symmetric structure of lower energy than those provided by our computations. However, the many defective structures found by our minimization apparently reflects the near degeneracy of many different geometries and spin configurations at the electron densities close to the Wigner transition. This feature is expected to be present also in real systems, and suggests that experiments might provide different results for seemingly
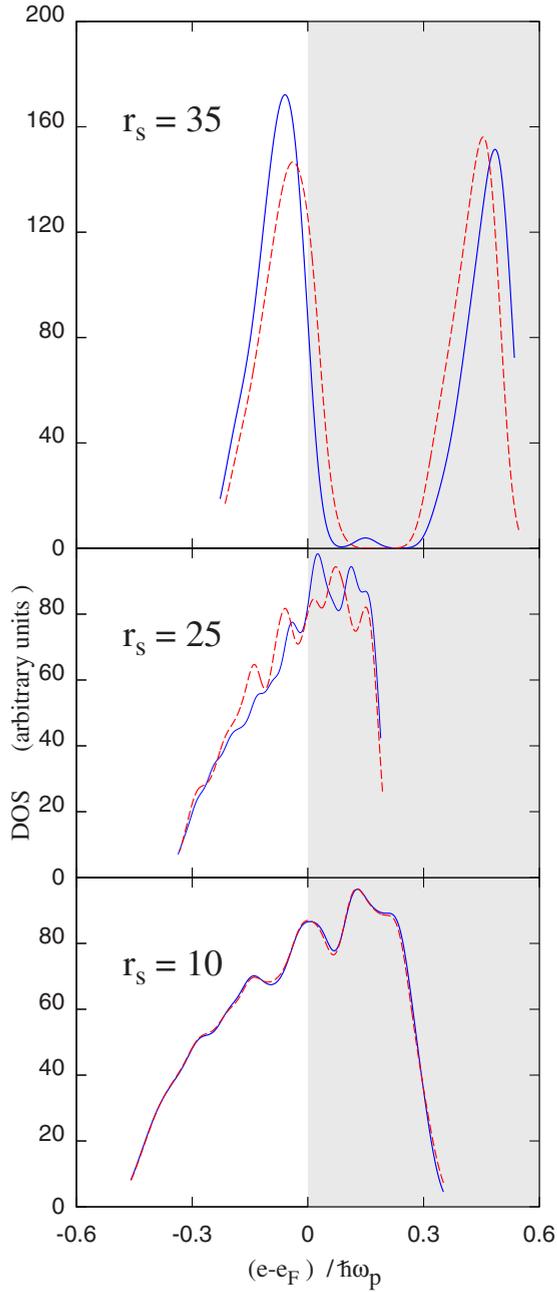
FIG. 12. (Color online) Spin-resolved density of states at r_s =10, r_s=25, and r_s=35. Blue full line: spin up states and Ref dash line: spin down states. The shaded area identifies empty states.

equivalent samples, a feature not uncommon in the physics of disordered materials.

The energy distribution of Kohn-Sham eigenvalues (density of states, DOS) is shown in Fig. 12 at three r_s values (r_s=10, 25, and 35) and N=700. In all cases, the cutoff of the DOS on the high-energy side is due to the finite number (N'=N) of empty states computed in our simulations (see Sec. I). At the highest density (r_s=10), the spin-up and spin-down components virtually coincide. For both spin-up and spin-down electrons, the energy dependence of the DOS is still reminiscent of the ideal OCP result, corresponding to a single parabolic band. At intermediate densities (r_s=25), small differences in the two spin-resolved DOSs point to the
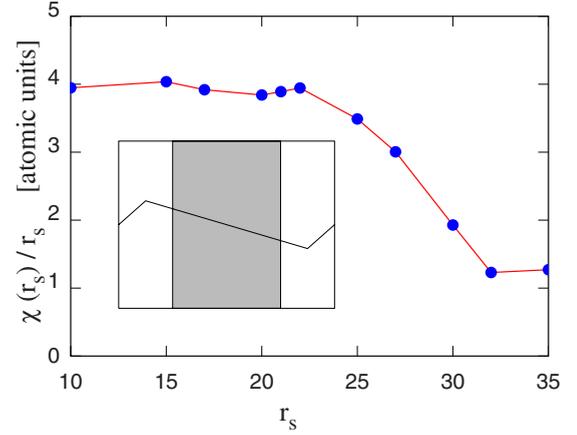
FIG. 13. (Color online) Dependence of the dipole polarizability per unit area on r_s (see text). The polarizability is measured along the direction z perpendicular to the slab surface. The inset shows the z dependence of the perturbing electrostatic potential with respect to the slab, whose location corresponds to the shaded area.

spontaneous spin polarization of the slab, and are due to the relatively disordered distribution of spins in space, and, in particular, to spin-polarized defects. Finally, at densities such that electrons are fully localized (r_s=35) in addition to being spin-polarized, the spin-up and spin-down DOSs present a multiple-peak structure (only two are visible in Fig. 12). In an apparent case of strong shell effects, the Fermi energy for the r_s=35, N=700 sample is not in the middle of the gap separating the low- and high-energy bands but it falls not far from the edge of the lowest-energy band. In all cases, however, the spin-resolved DOS only mildly reflects the spin-polarization transition while charge localization leaves a more apparent signature.

The metal-insulator transition accompanying the Wigner crystallization is expected to have a sizable effect on the electron polarizability of the slab. By definition, a conductor screens every electric field applied to the system, confining it to a thin skin layer. A planar slab immersed into a perpendicular field $\mathbf{E}=(0,0,E_z)$ will accumulate a surface charge $\sigma=E_z/4\pi$ of opposite sign on the two faces of the slab, thus acquiring a dipole moment $P_z=E_zL_z/4\pi$ per unit area. The slab polarizability in the z direction, therefore, will be proportional to L_z, and thus, in our computations, proportional to r_s.

The polarization of an insulator is still proportional to the system volume and thus the polarizability per unit area of a planar slab is also proportional to the slab thickness. In this case, however, the acquired dipole moment will be less than in the metallic case and the proportionality factor relating P to L_z will display a nontrivial dependence on r_s. As a result, χ will no longer be simply proportional to r_s. A plot of $\chi(r_s)/r_s$, therefore, is expected to display a nearly constant plateau at metallic densities and a progressive drop with r_s increasing beyond the Wigner crystallization point.

Such a behavior is seen precisely in Fig. 13, showing the plot of $\chi(r_s)/r_s$ as a function of r_s. As expected, across the metal-insulating transition the polarizability decreases from the extreme case of the conducting state. Also this observation could provide an additional, complementary diagnostic

quantity to characterize the transition in real systems.

Needless to say, the electron conductivity is the most obvious quantity to monitor in order to detect changes in the electronic structure at the Wigner crystallization that is expected to correspond also to the metal-insulator transition for the OCP. In the extended 3D case, application of the Kubo-Greenwood formula [see Eq. (10)], shows that conductivity consists only of a single, δ-like peak at zero frequency for all densities such that the electron density is uniform, and KS eigenstates are single plane waves. Conductivity at nonvanishing frequency arises around the localization transition, when each eigenstate becomes the superposition of many plane waves of different wave vector. Strict charge localization at higher r_s will prevent again conductivity, unless the frequency of the applied field is sufficient to promote electrons into extended states of fairly high energy.

In the case of our simulated slabs, the density and energy dependence of conductivity result from the interplay of charge localization, spin polarization, and band-filling effects. Because of the limited number of empty states determined in our computation, our discussion of conductivity is limited to the low-energy regime, corresponding to a fraction ($\sim 20\%$) of the bulk plasma frequency. The computation of conductivity in the plane xy parallel to the surface, carried out again with the Kubo-Greenwood formula of Eq. (10), shows that at densities such that the system is spin-unpolarized (see $r_s = 10$ in Fig. 14), the spin-up and spin-down channels are, as expected, equivalent. Moreover, the analysis of the spatial distribution of conductivity [see Eq. (15)] shows that the induced current is higher within the slab than in close proximity of the surfaces. The spontaneous spin polarization arising at $r_s = 25$ gives rise to a marked asymmetry in the two spin channels that tends to increase with decreasing density. Moreover, in systems such that charge is localized, conductivity tends to occur at the surface, as shown by the results for $r_s = 25$ in Fig. 14. In all cases, we observe a close correspondence between the distribution of induced current and structural features in the sample. The two inequivalent planar surfaces of the $r_s = 30$ sample shown in Fig. 11, for instance, display a markedly different conductivity in proximity of the two surfaces. More remarkably, conductivity in this sample takes place predominantly in the subsurface plane where the bcc-like and fcc-like lattices match, as described above. It is tempting to interpret these results as suggesting that conductivity in well-localized samples results from the many defects seen in the ground-state structures.

The results of computations for the fully spin-polarized sample at $r_s = 40$ and $N = N_{up} = 700$ electrons provide results completely analogous to those described above for $N_{up} = N_{down}$ systems, apart from obvious differences in magnetization structures, in band filling, and thus in conductivity.

III. SUMMARY AND CONCLUSIONS

The surface properties of the jellium model have been explored by large supercell computations in the DFT-LSD approach for planar slabs with up to 1000 electrons. A wide interval of densities ($10 \leq r_s \leq 40$) has been covered, extend-
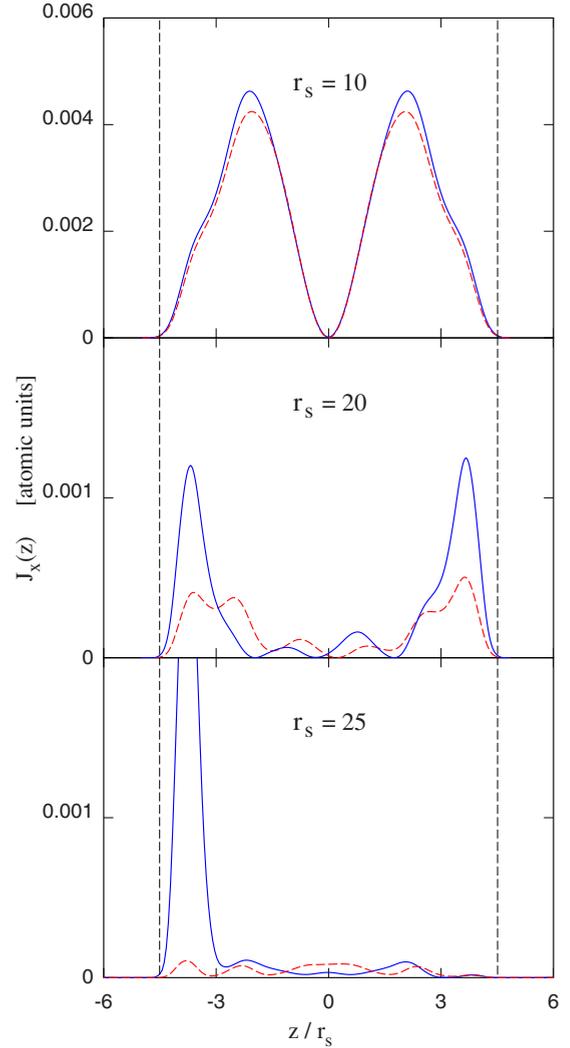
FIG. 14. (Color online) Spin- and z-resolved conductivities at $r_s = 10$, $r_s = 20$, and $r_s = 30$. Blue full line: spin up and red dash line: spin down. The dashed vertical lines mark the position of the background edge.

ing well into the stability range of the Wigner crystal. Following standard computational recipes, Kohn-Sham orbitals have been expanded on a large basis of plane waves, whose wave vector belongs to the reciprocal lattice of the supercell geometry. Most computations have been carried out for globally spin-compensated system, having $N_{up} = N_{down}$. Nevertheless, spin compensation is not enforced locally and polarization can arise as a way to lower the exchange energy. The influence of global spin compensation has been tested by a few computations for fully spin-polarized samples ($N_{up} = N, N_{down} = 0$) at $r_s = 40$, and found to be relatively minor.

The unconstrained minimization of the DFT-LSD functional with respect to these orbitals provides a direct view of changes in the surface properties across the transition from the paramagnetic electron fluid to the fully localized Wigner crystal. Spin polarization and in-plane charge modulation arise nearly simultaneously at the surface starting from $r_s \sim 20$. With decreasing density (increasing r_s) both polarization and charge modulation extend toward the center of the slab, at the same time enhancing their amplitude.

Starting from $r_s = 30$, the charge modulation has evolved into a clearly identifiable Wigner crystal consisting of rounded blobs of electron density, each corresponding nearly exactly to one electron and one (1/2) spin. A simple way to represent the lattice by associating particles to local density maxima has been proposed and the results are shown in Figs. 8–11. Analysis of the simulation results for the fully charge localized samples reveal both apparent regularities as well as many defects in the spatial distribution of blobs. We observe, in particular, surface vacancies, probably due to the mismatch between the actual slab size and the integer numbers corresponding to the filling of regular orthorhombic portions of the Wigner lattice, a feature that has been described as *shell effects* in the previous section. We observe also other point and extended defects such as dislocations and disclinations, familiar from the solid state physics of atomic lattices. In the case of electrons, some of these defects will give rise to tunneling centers, whose presence could manifest itself in spectroscopic data measured at very low temperature.

In most cases, the distribution of localized spins is too disordered to be described simply as the superposition of defects on an underlying regular structure. We find that spin disorder increases with decreasing density, paralleling the decrease in exchange energy in going toward more dilute systems.

The spin-resolved energy distribution of Kohn-Sham eigenvalues (DOS) is still reminiscent of the ideal OCP one in the paramagnetic liquid regime at $r_s = 10$, with spin-up and spin-down components virtually coinciding with each other. Local spin polarization and the first stages of charge localization ($20 \leq r_s \leq 25$) have only a limited impact on the density evolution of the DOS, which only displays relatively small differences between the spin-up and spin-down DOS components with oscillations superimposed to an otherwise monotonically increasing trend. The propagation of charge localization to the entire sample, instead, has a major effect, dividing both spin-up and spin-down DOSs into disjoint bands. Because of the shell effects described above, the precise position of the Fermi energy within a band or in between bands depends on the size N of the sample. For the systems considered in our simulations, for instance, sizes do not correspond to the precise filling of bands, and our systems, in many respects, behave as open shell systems. This is reflected, for instance, into a residual but still sizable conductivity parallel to the surface even at $r_s \geq 30$, which is limited only by charge localization (and not by band effects). Detailed analysis of the current induced by an external field parallel to the surface shows that in charge-localized systems ($r_s \geq 30$) conductivity is a surface property. We have been unable to verify unambiguously that surface conductivity is mediated by surface vacancies but it is tempting to assume that this is indeed the case. A qualitative link between conductivity and surface vacancies is established by the observation that surface vacancies arise primarily from the incomplete filling of electron layers (shell effect), which, in turn, is responsible for the location of the Fermi energy inside one of the bands.

At all densities such that local spin polarization is present, the in-plane conductivity is apparently asymmetric in the two spin channels. This is an interesting observation from the conceptual point of view and it could be even more important in practice, especially in view of spintronics applications. In the case of fully localized samples, we found cases in which the two surfaces of the planar slab are apparently different (see Fig. 11). In these cases, the structural anomaly is reflected into an equally apparent asymmetry of the conductivity associated to the two surfaces.

Finally, we identified a few additional changes in the density dependence of the surface energy, in the electrostatic polarizability perpendicular to the surface and in the electron spill out from the jellium background that mark the transition to the fully localized state.

All these observation provide a wealth of features and predictions on the properties of low-density jellium surfaces and of Wigner crystal surfaces, in particular. Of course, the picture provided by our computations concerns the DFT-LDA level of approximation. Semilocal approximations such as gradient-corrected DFT recipes are not likely to change the picture.[31] Fully correlated and virtually exact computations relying, for instance, on quantum Monte Carlo might provide a different picture. These computations, however, are not available yet, and might not be easy to carry out[18] at the level of accuracy required to quantitatively characterize surface properties of low-density slabs. In the meantime, computational studies based on DFT approximations are the most accessible route to obtain a first view of Wigner crystal surfaces that could assist setting-up experiments and interpreting their data. Moreover, the results accumulated during this stage provide a clear set of predictions to be validated or disproved by more sophisticated methods whenever they will become available.

---

[1] G. Giuliani and G. Vignale, *Quantum Theory of the Electron Liquid* (Cambridge University Press, Cambridge, 2005).

[2] N. W. Ashcroft and N. D. Mermin, *Solid State Physics* (Holt-Saunders, London, 1976).

[3] E. Kaxiras, *Atomic and Electronic Structure of Solids* (Cambridge University Press, Cambridge, 2003).

[4] L. D. Landau, Sov. Phys. JETP **3**, 920 (1957); **5**, 101 (1957); **8**, 70 (1959).

[5] E. Wigner, Phys. Rev. **46**, 1002 (1934).

[6] W. M. C. Foulkes, L. Mitas, R. J. Needs, and G. Rajagopal, Rev. Mod. Phys. **73**, 33 (2001).

[7] D. M. Ceperley and B. J. Alder, Phys. Rev. Lett. **45**, 566 (1980).

[8] G. Ortiz, M. Harris, and P. Ballone, Phys. Rev. Lett. **82**, 5317 (1999).

[9] J. C. Fernandes, R. B. Guimaraes, M. A. Continentino, L. Ghivelder, and R. S. Freitas, Phys. Rev. B **61**, R850 (2000).

[10] J. Yoon, C. C. Li, D. Shahar, D. C. Tsui, and M. Shayegan, Phys. Rev. Lett. **82**, 1744 (1999).

[11] V. V. Deshpande and M. Bockrath, Nat. Phys. **4**, 314 (2008).

[12] A. Rahman and M. K. Sanyal, Phys. Rev. B **76**, 045110 (2007).

[13] J. Bardeen, Phys. Rev. **49**, 653 (1936).

[14] N. D. Lang and W. Kohn, Phys. Rev. B **1**, 4555 (1970); **3**, 1215 (1971).

[15] J. M. Pitarke and A. G. Eguiluz, Phys. Rev. B **63**, 045116 (2001).

[16] J.-M. Tao, J. P. Perdew, L. M. Almeida, C. Fiolhais, and S. Kümmel, Phys. Rev. B **77**, 245107 (2008).

[17] X.-P. Li, R. J. Needs, R. M. Martin, and D. M. Ceperley, Phys. Rev. B **45**, 6124 (1992).

[18] B. Wood, N. D. M. Hine, W. M. C. Foulkes, and P. Garcia-Gonzalez, Phys. Rev. B **76**, 035403 (2007).

[19] E. Krotscheck and W. Kohn, Phys. Rev. Lett. **57**, 862 (1986).

[20] F. H. Zong, C. Lin, and D. M. Ceperley, Phys. Rev. E **66**, 036703 (2002).

[21] N. D. Drummond, Z. Radnai, J. R. Trail, M. D. Towler, and R. J. Needs, Phys. Rev. B **69**, 085116 (2004).

[22] An early theoretical study, however, predicted the Wigner crystal to be antiferromagnetic, at least up to $r_s \sim 270$. See: W. J. Carr, Phys. Rev. **122**, 1437 (1961).

[23] L. Cândido, B. Bernu, and D. M. Ceperley, Phys. Rev. B **70**, 094413 (2004).

[24] A. Zangwill, *Physics at Surfaces* (Cambridge University Press, Cambridge, 1988).

[25] B. Tanatar and D. M. Ceperley, Phys. Rev. B **39**, 5005 (1989); F. Rapisarda and G. Senatore, Aust. J. Phys. **49**, 161 (1996); C. Attaccalite, S. Moroni, P. Gori-Giorgi, and G. B. Bachelet, Phys. Rev. Lett. **88**, 256601 (2002).

[26] K. Okazaki and Y. Teraoka, Phys. Rev. B **62**, 500 (2000); Y. Ito and Y. Teraoka, Solid State Commun. **127**, 275 (2003); K. Okazaki and Y. Teraoka, *ibid.* **116**, 269 (2000); Surf. Sci. **433-435**, 672 (1999).

[27] Y. Ito and Y. Teraoka, J. Magn. Magn. Mater. **272-276**, E237 (2004); K. Okazaki and Y. Teraoka, Appl. Surf. Sci. **169-170**, 48 (2001); Solid State Commun. **114**, 215 (2000).

[28] R. M. Méndez-Moreno, M. A. Ortiz, S. Orozco, and M. Moreno, Solid State Commun. **121**, 223 (2002).

[29] G. Senatore and G. Pastore, Phys. Rev. Lett. **64**, 303 (1990).

[30] J. R. Trail, M. D. Towler, and R. J. Needs, Phys. Rev. B **68**, 045107 (2003).

[31] Y. Ito and Y. Teraoka, J. Magn. Magn. Mater. **310**, 1073 (2007).

[32] J. P. Perdew and A. Zunger, Phys. Rev. B **23**, 5048 (1981).

[33] F. Sottile and P. Ballone, Phys. Rev. B **64**, 045105 (2001).

[34] D. Marx and J. Hutter in *Modern Methods and Algorithms of Quantum Chemistry*, NIC Series Vol. 1, edited by J. Grotendorst (John von Neumann Institute for Computing, Jülich 2000), pp. 301–449.

[35] W. H. Press, B. P. Flannery, S. A. Teukolsky, and W. T. Vetterling, *Numerical Recipes: The Art of Scientific Computing* (Cambridge University Press, Cambridge, 1986).

[36] J. Vannimenus and H. F. Budd, Phys. Rev. B **15**, 5302 (1977).

[37] R. Resta, L. Colombo, and S. Baroni, Phys. Rev. B **41**, 12358 (1990).

[38] K. J. Strandburg, Rev. Mod. Phys. **60**, 161 (1988).